

Article - Human and Animal Health

Biogran Grafting in Rat Tibia Defects – A Model of High Bone Metabolism Site

Luiza de Almeida Queiroz Ferreira¹
https://orcid.org/0000-0002-5534-9432

Luiz Felipe Cardoso Lehman²
https://orcid.org/0000-0001-6404-1766

Marina Gonçalves Diniz³
https://orcid.org/0000-0002-4212-1172

Anderson José Ferreira⁴
https://orcid.org/0000-0002-3915-3691

Rosangela Maria Ferreira da Costa e Silva^{6*}
https://orcid.org/0000-0002-6792-2558

Tarcília Aparecida Silva²
https://orcid.org/0000-0001-9623-7835

Ricardo Alves Mesquita²
https://orcid.org/0000-0003-3207-4007

Rafaela Férrer de Oliveira¹
https://orcid.org/0000-0001-6572-5895

Mariana Saturnino Noronha²
https://orcid.org/0000-0001-9188-1939

Daniel Marques Leão¹
https://orcid.org/0000-0001-6512-116X

Ângela Leão Andrade⁵
https://orcid.org/0000-0002-0888-5072

Rosana Zacarias Domingues⁷
https://orcid.org/0000-0001-5667-2031

Ivana Márcia Alves Diniz¹
https://orcid.org/0000-0003-4261-0037

¹Universidade Federal de Minas Gerais, Faculdade de Odontologia, Departamento de Odontologia Restauradora, Belo Horizonte, Minas Gerais, Brasil; ²Universidade Federal de Minas Gerais, Faculdade de Odontologia, Departamento de Patologia e Cirurgia Oral, Belo Horizonte, Minas Gerais, Brasil; ³Universidade Federal de Minas Gerais, Instituto de Ciências Biológicas, Departamento de Patologia, Belo Horizonte, Minas Gerais, Brasil; ⁴Universidade Federal dos Vales do Jequitinhonha e Mucuri, Faculdade de Medicina, Diamantina, Minas Gerais, Brasil; ⁵Universidade Federal de Ouro Preto, Departamento de Química, Ouro Preto, Minas Gerais, Brasil; ⁶Universidade Estadual de Mato Grosso do Sul, Dourados, Mato Grosso do Sul, Brasil; ⁷Universidade Federal de Minas Gerais, Departamento de Química, Belo Horizonte, Minas Gerais, Brasil.

Editor-in-Chief: Paulo Vitor Farago
Associate Editor: Fábio André dos Santos

Received: 01-Jan-2023; Accepted: 07-Sep-2023

*Correspondence: rosangela_ferreirafeliz@yahoo.com.br; Tel: +55 41 9926 16062 (R.M.F.C.S.).

HIGHLIGHTS

- The surface area of the material was 0.2653 m² g⁻¹.
- After three days immersed in *SBF solution*, bands at 604 and 563 cm⁻¹ were detected.
- Biogran has stimulated sustained levels (130–200 pg/100mg) of BMP-2.
- Bone formation was similar or significantly higher in the Biogran groups than in autogenous grafting.

Abstract: We investigated the Biogran on bone repair and metabolism at several time-intervals upon grafting into rat tibia artificial defects. The biomaterial was thoroughly characterized *in vitro*, and its dissolution behavior upon immersion was assessed in simulated body fluid (SBF) solution for 1, 3, 7, 14, and 30 days. Biogran was also assessed by *in vitro* hydroxyapatite formation in SBF solution, which is a marker for bioactive behavior. *In vivo*, distal and proximal bone defects were performed in the Wistar rat's right tibia and filled according to the experimental groups: I) negative control, no filling; II) positive control, 10 mg of autogenous bone; and III) 10 mg of Biogran. Animals were euthanized at 1, 2, 3, 4, 7, and 10 weeks. Bone neoformation was analyzed using histomorphometry (proximal defect), and local levels of bone morphogenetic protein 2 (BMP-2) were measured using the ELISA assay (distal defect). *In vitro*, the Biogran sample showed a fast dissolution rate within the first 7 days, parallel to the formation of the hydroxyapatite layer. *In vivo*, the sample was progressively resorbed at a higher rate within the first month until it became almost absent at week 10th. The sample presented similar or higher bone neoformation concerning the autogenous bone. BMP-2 levels were sustained in the Biogran group (around 200 pg/mg) and detected until the last experimental time with a significant difference compared with the controls. Results suggest Biogran is a candidate for hard tissue engineering even in highly active bone remodeling sites.

Keywords: Biogran; Bone Regeneration; Bone Morphogenetic Protein 2; Tibia.

INTRODUCTION

Scaffolds made of bioactive glasses are rich in interconnected porous structures similar to the trabecular bone. These biomaterials may work as a temporary template for cells to grow into, thus aiding the regeneration process in hard tissues [1, 2]. The first bioactive glasses were developed by Hench and colleagues in 1969, and since then, these biomaterials are continuously refined to attend the ability to integrate living tissues and to induce the growth of neoformed tissues [3-5].

Several glasses, especially in the quaternary system $\text{Na}_2\text{O}-\text{CaO}-\text{P}_2\text{O}_5-\text{SiO}_2$, are known to be bioactive or degradable in contact with biological environments. The most prominent example is the composition termed Bioglass 45S5 [4]: that consists of 45 wt% SiO_2 , 24.5 wt% CaO , 24.5 wt% Na_2O , and 6 wt% P_2O_5 , and is produced by conventional melt-quenching route. The Bioglass 45S5 is not the only product on the market. Biogran (Biomet 3i Innovations Inc., Palm Beach Gardens, FL) has the same composition as Bioglass and is produced by melt, but with a narrower (300–360 μm) particle size range [6].

Bioactive glasses are reported to be able to stimulate more bone regeneration than other bioactive ceramics [6]. Hench proposed a mechanism to explain the bonding of 45S5 Bioglass to soft and hard tissue comprising five material-based sequences and six steps on the cellular level [7-9]. Briefly, it can be summarized that, upon contact to a physiological environment, the glass surface releases network modifiers, namely sodium and calcium ions, leading to an increase in local pH and supersaturation with respect to hydroxyapatite. Due to the pH increase, the glass surface is hydrolyzed, leading to a highly porous silica gel layer. After adsorbing Ca^{2+} and PO_4^{3-} species from the surrounding biological fluid, the crystallization of the hydroxyapatite layer takes place [10, 11]. The release of water-soluble ionic species from the crystalline hydroxyapatite layer, especially silica and calcium compounds, are bioactive on the cellular level: The sublayer of silica adheres tightly to the bone's apatite crystals [12] and they behave like growth factors, providing signals to the host progenitor stem cells leading to bone neoformation [1, 13, 14]; both, mitosis of osteoprogenitor cells [15] and angiogenesis [16] are stimulated.

Several properties of bioactive glasses make them desired substitutes for autogenous bone grafts. Although bone neoformation has achieved the gold standard by using the host's bone replacement, one of the main drawbacks in these procedures is the need for a second surgical site for bone donation [17]. Secondary surgical sites are at risk of infection and increase the procedure morbidity, lowering the patient's quality of life [18, 19]. Another main issue in these procedures is that a donation area is limited or not available [20]. Synthetic biomaterials may then be synthesized to be mechanically resistant to support new tissue growth, at least temporarily [21, 22].

Previous studies have evaluated Biogran's behavior as a bone grafting material [14, 23-29]. Most of them have shown promising results regarding the use of the biomaterial in maxillary sinus augmentation and their participation in bone formation around implants [23, 25, 26, 29]. Regardless of the notorious ability of the Biogran for bone neoformation, the time for the total sample resorption is barely predictable in active bone remodeling sites. As such, a scaffold's low degradation or high resorption rates may delay the new bone formation and healing processes [30]. Heretofore, none of the Biogran studies have followed up the grafting of this biomaterial for several time points verifying its application as a bone alternative in highly metabolic

conditions, such as tibial defects. Furthermore, little is known about Biogran local stimulation of pro-osteogenic growth factors, such as bone morphogenetic proteins (BMP). BMP's are associated with the differentiation of mesenchymal stem cells into osteoblasts, playing a fundamental role in the bone neoformation process [31]. These same proteins have direct and indirect action (RANKL and osteoprotegerin) on osteoclastic cells, thus modulating bone resorption [32]. Despite the recognized advantageous characteristics of Biogran as bone grafting material, we hypothesized that the biomaterial would present limited application in long bones. Accordingly, the present study's main purpose was to investigate the Biogran bone repairing ability upon grafting into surgical defects performed in Wistar rats' tibia. The biomaterial grafting was molecular and histologically compared to autogenous bone or no treatment along six experimental times, from the first month to the 10th week. We also correlated the *in vivo* findings with a comprehensive *in vitro* characterization of the Biogran.

MATERIAL AND METHODS

Materials

In vitro studies

Biogran particles were obtained from Biomet 3i Innovations Inc. (Palm Beach Gardens, FL, USA).

Scanning Electron Microscopy (SEM) and Energy Dispersive Spectroscopy (EDS)

The morphology and microstructure of the Biogran were analyzed by SEM (FEG – Quanta 200 FEI, Hillsboro, OR, USA) coupled with EDS. Samples were inserted on aluminum stubs and sputter-coated with a thin layer of gold (approximately 45 μm). EDS was used to evaluate elemental composition semi-quantitatively [33, 34].

Surface area by the gas adsorption analysis (B.E.T method)

Nitrogen adsorption/desorption analyzes were performed to assess the specific surface area and porosity of the Biogran. Samples (0.1025 g) previously degassed at 150 °C for 8 h under vacuum conditions using an Autosorb 1200 equipment (Quantachrome Instruments Boynton Beach, USA). BET (Brunauer, Emmett, Teller) method was used by calculated the specific surface area within the pressures range of 0.05–0.30 [35].

X-ray Fluorescence (XRF)

XRF was used to provide compositional analysis of the Biogran (Shimadzu, XRD-7000 X-RAY diffractometer, Kyoto, Japan), using Co(K α) radiation [36, 37].

X-ray Diffraction (XRD)

X-Ray Diffraction (XRD) was performed in a diffractometer (Shimadzu, Model XRD-6000, Tokyo, Japan) equipped with a Cu(K α) radiation (1.54184 Å, 40 kV and 30 mA) and monochromator graphite. Diffractogram were obtained with an angle between 15° and 70 ° 2 θ , and a scanning speed of 1° 2 θ /min [36].

Fourier Transform Infrared Spectroscopy (FTIR) and *in vitro* bioactivity evaluation

FTIR (Perkin Elmer FTIR GX, Wellesley, MA, USA) spectra of the Biogran before and after the immersion of SBF solution were evaluated. The solids were homogenized in KBr (2% w/w), and disc pressed. The spectra were recorded with a resolution of 4 cm^{-1} with 32 scans in the range of 400-4,000 cm^{-1} . The *in vitro* bioactivity evaluation was conducted by placing the samples into polyethylene vials with simulated body fluid (SBF) solution kept at 37 °C. A sampling ratio of 0.002 g cm^{-3} (w/v) was used in each experiment with an incubation period of 1, 3, 7, and 21 days (n=3). During the incubation period, the SBF solution was replaced every other day. The formation of hydroxyapatite (HA) layer was monitored through FTIR. The kinetics of HA formation in SBF solution was semi-quantitatively evaluated by plotting the ratio of the intensity (I_1) of the vibration band at about 560 cm^{-1} [corresponding to HA (P-O)], and the intensity (I_2) of the silica (Si-O) mode at 1025 cm^{-1} versus time. The results were expressed as intensity ratio I_1/I_2 [38, 39].

Dissolution test

In order to evaluate the sample *in vitro* dissolution, Biogran samples were immersed into SBF in a ratio equal to 0.2 % (w/v) and incubated at 37 °C (n=3). After 1, 3, 7, 14 and 30 days, the samples were removed from SBF, rinsed with deionized water, and dried at 60 °C. Prior to immersion and after the removal of the dissolution products, the samples were weighed. The difference between these two values was used to determine the weight loss [10, 11].

In vivo studies

The Ethical Committee for Animals Use of the Universidade Federal de Minas Gerais approved this study (protocol #103/2014). The study was conducted according to the Animals Research: Reporting of *In Vivo* Experiments (ARRIVE) guidelines. Ninety male Wistar rats (7 to 8 weeks, 250-350 g) were used (n=5 per group, per experimental time) after sample size calculation using bone neoformation quantification through histology as the most unstable variable [40]. All animals were kept under climate-controlled conditions, with *ad libitum* access to water and feed.

Surgical Procedures and Experimental Groups

Randomization was performed at six experimental times, each containing 15 animals, through homogenous distribution of animals by weight two weeks before experiments. One animal from each group was performed sequentially until n=15 in an experiment time. One animal from each group was performed sequentially until n=15 in an experiment time, obeying the following order: negative control, autogenous bone, and Biogran grafting. All surgical procedures were performed under anesthesia (xylazine 15 mg kg⁻¹ and ketamine 100 mg kg⁻¹; Rhobifarma Indústria Farmacêutica Ltda, São Paulo, SP, Brazil). A 10-mm incision was made over the tibial crest of the animals under anesthesia. The soft tissue detachment was performed with the aid of a Hollenback 3S instrument (SSwhite/Duflex, Rio de Janeiro, RJ, Brazil), and two bone defects were then performed with a helical drill on the tibia (1.6 mm in diameter; Neodent, Curitiba, PR, Brazil). The defects were filled according to the experimental groups: I) negative control, no filling; II) positive control, 10 mg of autogenous bone collected from the animal's right tibia; and III) Biogran, 10 mg of the sample. After the surgical procedure, the wounds were closed with 5.0 thread (Ethicon, Johnson & Johnson, São José dos Campos, São Paulo, SP, Brazil). The five animals from a group and experimental time were housed in the same cage. The animals were medicated with 0.1 mL of intramuscular flunixin (Benamine, Schering-Plow Animal Health, Harefield, United Kingdom), 12/12 hours for three days, for post-operative comfort.

Euthanasia

The animals were euthanized at weeks 1, 2, 3, 4, 7, and 10 post-operatively with anesthesia overdose (xylazine 45 mg kg⁻¹ and ketamine 300 mg kg⁻¹). The soft tissue covering the tibia was removed with a diamond disc (KG Sorensen, Cotia, SP, Brazil), separating the two defects. The proximal defect was fixed in a 10% buffered neutral formalin solution (pH 7.2) and was subsequently decalcified (ethylenediaminetetraacetic acid – EDTA 10%, pH 7.4, for 4 weeks) and embedded in paraffin. The distal defect was immersed in phosphate-buffered saline (0.4 mM NaCl, 10 mM NaPO₄, pH 7.4) containing protease inhibitors (0.1 mM phenylmethylsulfonyl fluoride, 0.1 mM benzethonium chloride, 10 mM EDTA, 0.01 mg/mL aprotinin A and 0.05% Tween 20) in the proportion of 1 mL of solution for 100 mg of tissue. The samples were weighed and ground using a homogenizer (PowerGen Model 1000 Homogenizer, Fisher Scientific, Loughborough, United Kingdom). After centrifugation (800 x g, 4 °C), the supernatant was collected and stored at -80 °C.

Histological and histomorphometry analyses

Longitudinal sections were obtained from samples with a thickness of 6 µm. Each sample was cut in half before being embedded in paraffin and then stained with hematoxylin and eosin (H&E) for routine histological analysis. The intensity of the inflammation was graded according to Schallenger and coauthors [41], and classified as none, mild, moderate, or severe by a blinded examiner (R.A.M.). In the first sections obtained, histomorphometry was performed by another blinded examiner (L.F.C.L.). The samples were stained for routine Masson's trichrome and analyzed under an optical microscope (Standard 25, Carl Zeiss, Göttingen, Germany). Bone quantification was performed using the ZEN 2 program (Carl Zeiss Microscopy, Jena, Germany). The measurements were made in areas occupied by newly formed bone in the defect regions, according to Lehman and coauthors [1].

Kinetics assessment of bone morphogenetic proteins (BMP-2)

The concentration of bone morphogenetic protein 2 (BMP-2) was determined in the samples collected at each experimental time using the enzyme-linked immunosorbent assay – ELISA (R&D Systems, Minneapolis, MN, USA), performed according to the manufacturer's instructions. The analysis was performed at a wavelength of 492 nm, and data were determined using a standard curve. Results were expressed in picograms per 100 mg of tissue.

Statistical Analysis

The Shapiro-Wilk test was performed to evaluate if the data had a normal distribution. Comparisons between experimental groups were performed using one-way ANOVA variance tests with Tukey's post-hoc in the GraphPad Prism 7.0 software (GraphPad Prism Version 7.0 for Mac, GraphPad Software, La Jolla, CA, USA). Data were expressed using means and standard deviations. The level of significance was defined as $p < 0.05$.

RESULTS

In vitro studies

Biogran powders' characterizations

Biogran powders' as received (Biogran) are depicted in Figure 1a. SEM analysis showed that Biogran is a particulate biomaterial composed of non-uniform polygonal granules presenting a smooth and dense surface texture (Figure 1b-1e). EDS analysis revealed the presence of Si, Ca, Na, and P (Figure 1f). The surface area of the material was of $0.2653 \text{ m}^2 \text{ g}^{-1}$ and the total pore volume was $0.00062 \text{ cm}^3 \text{ g}^{-1}$. The EDS (Figure 1e) and XRF (Table 1) analysis possibilities the confirmation of the qualitative and quantitative commercial composition (Figure 1e).

Table 1. Chemical composition of the Biogran determined by X-ray fluorescence (XRF) analysis.

Chemical species	CO ₂	Na ₂ O	SiO ₂	P ₂ O ₅	CaO
Biogran (wt. %)	0.74	24.8	41.4	5.6	27.2

XRD revealed a non-crystalline typical diffraction pattern for the Biogran (Figure 2a). Biogran spectra shows the broad amorphous crest, which covers the 2θ range from 20° through 35° , that is related to an amorphous silica gel network [42].

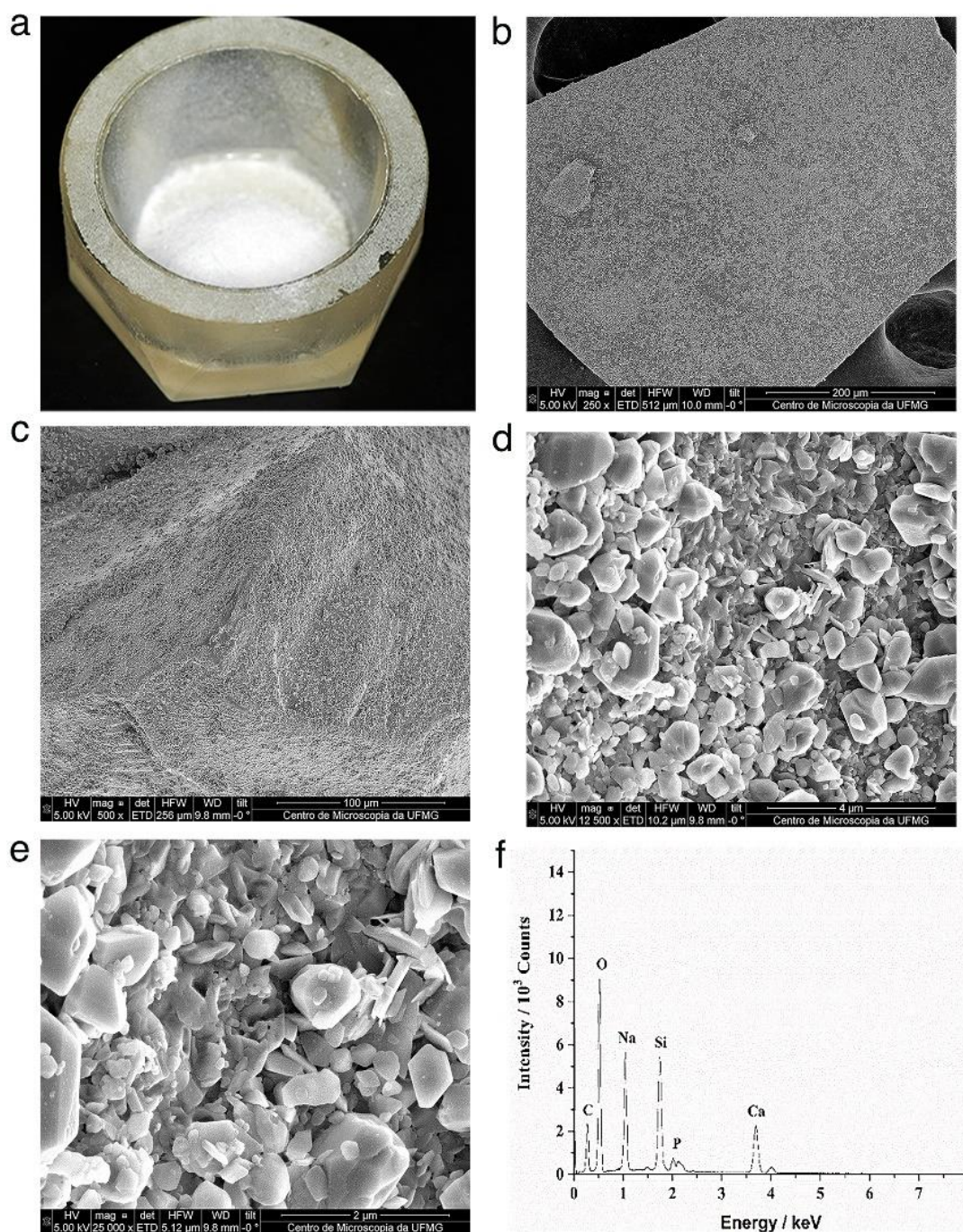


Figure 1. Biogran macro and microscopic morphologies. Biogran granules (a); SEM photomicrographs showing the surface of Biogran particles at a magnification of 250x (b), 500x (c), 12,500x (d); 25,000 (e); EDS of Biogran (f).

Biogran *in vitro* bioactivity evaluation

FTIR analysis of the Biogran demonstrated characteristic spectra (Figure 2b, a'). The band near 500 cm^{-1} corresponds to a Si–O rotation and bending mode; the band at 728 cm^{-1} corresponds to bending of Si–O; the band at 913 cm^{-1} is thought to be due to either Si–O–Ca, Si–O–Na, or non-bridging oxygen (NBO) [31]; and finally, the band at 1025 cm^{-1} corresponds to stretching of the Si–O bond [39]. After 1 day immersion in SBF (Figure 2b, b') disappeared a broad band between 500 and 600 cm^{-1} and appeared a band at 604 cm^{-1} . After 3 days immersed in SBF solution (Figure 2b, c') the bands at 604 and 563 cm^{-1} were detected, which could be assigned to the P–O stretching and bending modes in the (PO_4) tetrahedra (Figure 2b, c'). Those bands are characteristic of presence of hydroxyapatite (HA) and their intensities increased after more extended immersion periods (Figures 2b, d' and e'). There was also the appearance of the band at 460 cm^{-1} , and the intensity of the NBO vibration drops; and the band at 1050 cm^{-1} is covered within an extremely broad band centered at around 1000 cm^{-1} .

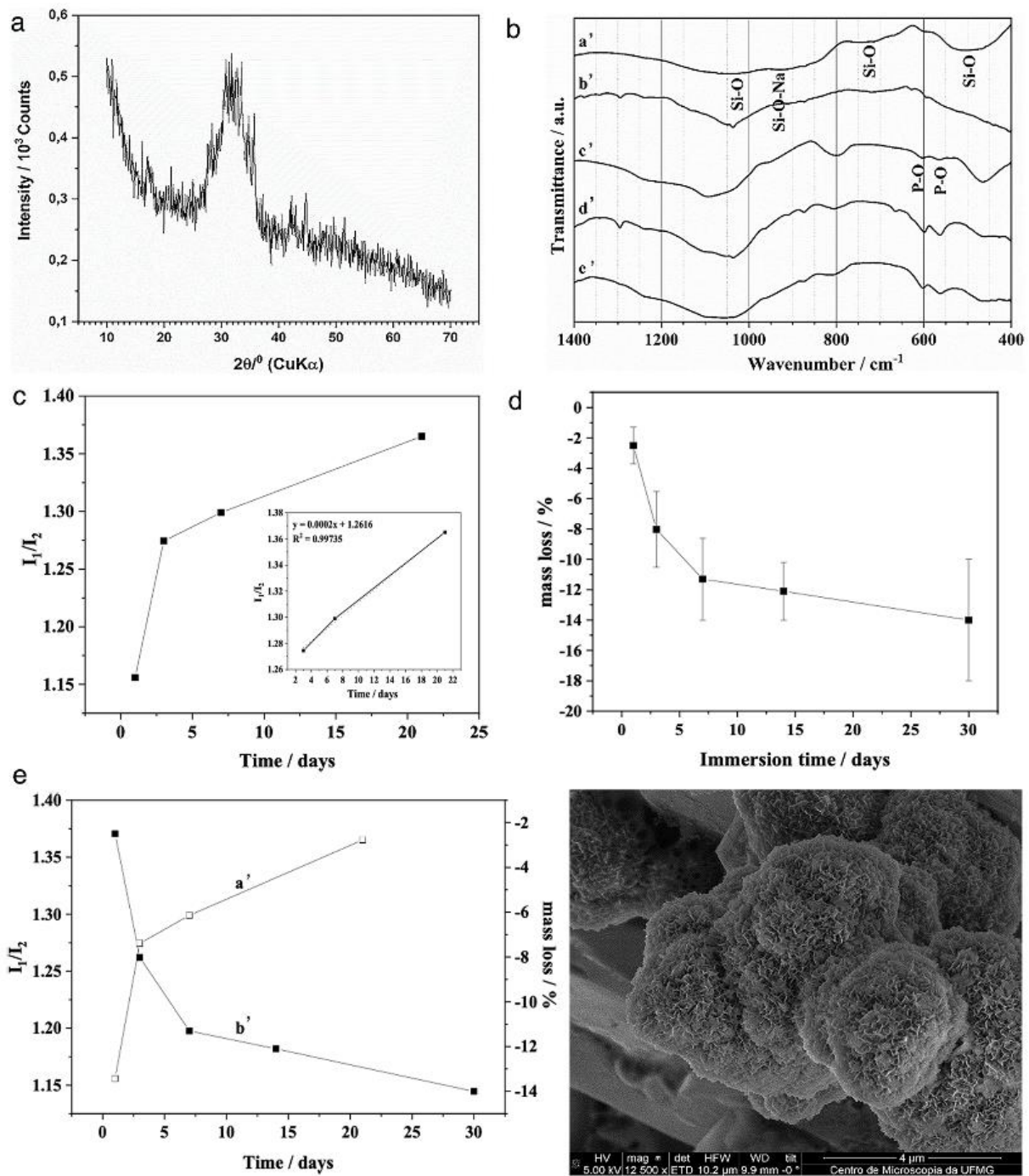


Figure 2. Biogran characteristics of non-crystalline materials and bioactivity. X-ray diffraction patterns of Biogran sample (a); Biogran FTIR spectra (a') before and after immersion in SBF for: (b') 1, (c') 3, (d') 7, and (e') 21 days (b); Biogran bioactivity as a function of HA formation in SBF measured as the ratio I_1/I_2 (c). The dissolution graph merged with the HA layer formation kinetics (d). Biogran bioactivity as a function of HA formation in SBF measured as the ratio I_1/I_2 (e, a'). The dissolution rate of the Biogran immersed in SBF solution (e, b'). SEM photomicrograph of Biogran at the magnification of 12,500x after 7 days immersion in SBF (f). It is possible to see numerous small needles like aggregates/crystals.

Moreover, the increase of this bands is observed at posteriorly until the time of 21 days (Figures 2b, d' and e'). The Biogran bioactivity as a function of HA formation in SBF solution and the sample' dissolution rate (I_1/I_2) is depicted in Figures 2c, d and e. The kinetics of HA formation in SBF solution was evaluated by the ratio of the of the vibration band at about 560 cm^{-1} [corresponding to HA (P-O)] intensity (I_1), and the silica (Si-O) mode at 1025 cm^{-1} (I_2) versus time (Figure 2c and e). There is an increase of I_1/I_2 . SEM of the Biogran after 21 days immersed show notes small needle-like particles possibly related to the formation of HA (Figure 2f).

Dissolution test

Results of dissolution tests for the Biogran at times of 3, 7, 14 and 21 days are shown in the Figures 2c-f. The mass loss was fast up to 3 days (Figure 2d, 2e) and after time happened dissolution at a lower rate. The dissolution data showed that the rate of hydroxyapatite formation on Biogran powders was proportional to the powders' dissolution in solution.

In vivo studies

No differences regarding the inflammation intensity and graduation were observed between Biogran and the other groups

The hematoxylin and eosin (H&E) staining for all groups is depicted in Figure 3. The inflammatory infiltrate was mild to moderate in all groups and surgical times where bone substitutes were present. The inflammatory infiltrate was classified as none in sites without the biomaterial or newly formed bone. The presence of giant/multinucleated cells was observed in the negative control at week 1 and in the positive control at weeks 1 and 2. These cells were present in the Biogran groups at weeks 1, 2, 4 and 7.

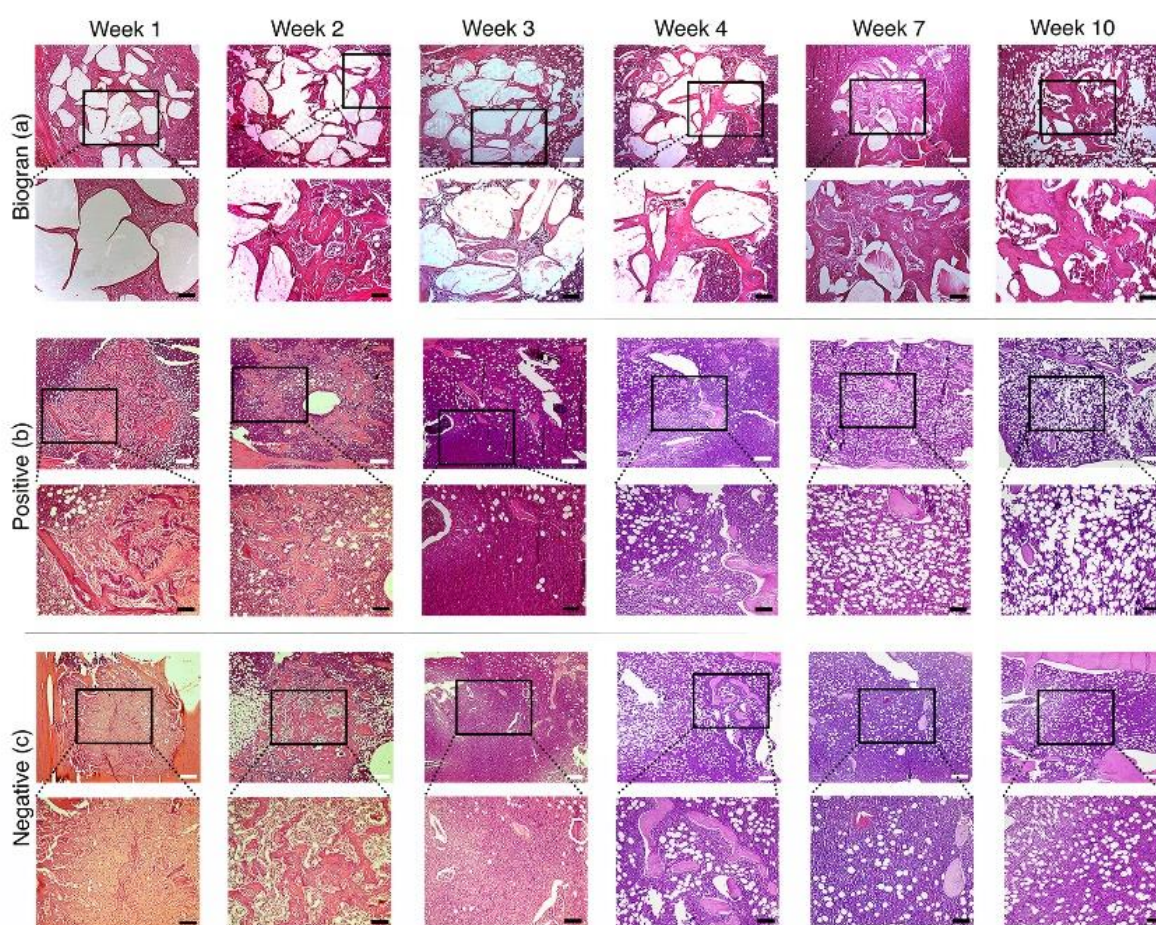


Figure 3. Representative H&E staining for the Biogran, positive and negative groups. Color bright-field photomicrographs at magnifications of 4x and 10x (4x image squared region) of Biogran (a), positive (b), and negative (c) groups from the first to the 10th week. Note that negative images within the surgical site correspond to the filled biomaterial. Black magnification scale bars = 100 μm; while white bar = 200 μm.

Biogran confers sustained bone formation

The Masson's trichrome staining is depicted in Figure 4a. At week 1, all groups were similar in the amount of bone formation, differing only by the presence of autogenous bone or biomaterial particles grafted in the positive and Biogran groups, respectively (Figure 4b). Lamellae bone formation could be seen in close contact with the grains of the biomaterial. At week 2, bone formation was numerically higher for the Biogran concerning the control groups but statistically different only regarding the negative control group ($p < 0.0001$)

(Figure 4b). Despite that, at this experimental time, the grafted autogenous bone was not easily found. For the Biogran group, the biomaterial grains were observed closely with a trabecular bone (Figure 4a). At week 3, the bone in the negative control group had been remodeled, and only native hematopoietic tissue from the tibial cord region was present at the site. The autogenous bone was also reabsorbed, and the newly formed bone was present in little amount. Biogran was still present at week 3, although the connective tissue was already being replaced by local hematopoietic tissue (Figure 4a). Bone formation was significantly higher in the Biogran groups concerning the controls at this experimental time (Figure 4b). Of note, Biogran granules appeared with newly formed bone in contact with these granules at weeks 3 and 4 (Figure 4a). At week 7, the positive and negative control groups presented a histological aspect compatible with the original hematopoietic tissue typical from long bones – such as the tibia, while the Biogran presented a remarkable amount of bone formation ($p < 0.001$) (Figure 4a and b). At week 10, both control groups were unchanged, while Biogran residues still appeared in close contact with a higher number of new bone lamellae ($p < 0.022$) (Figures 4a and b).

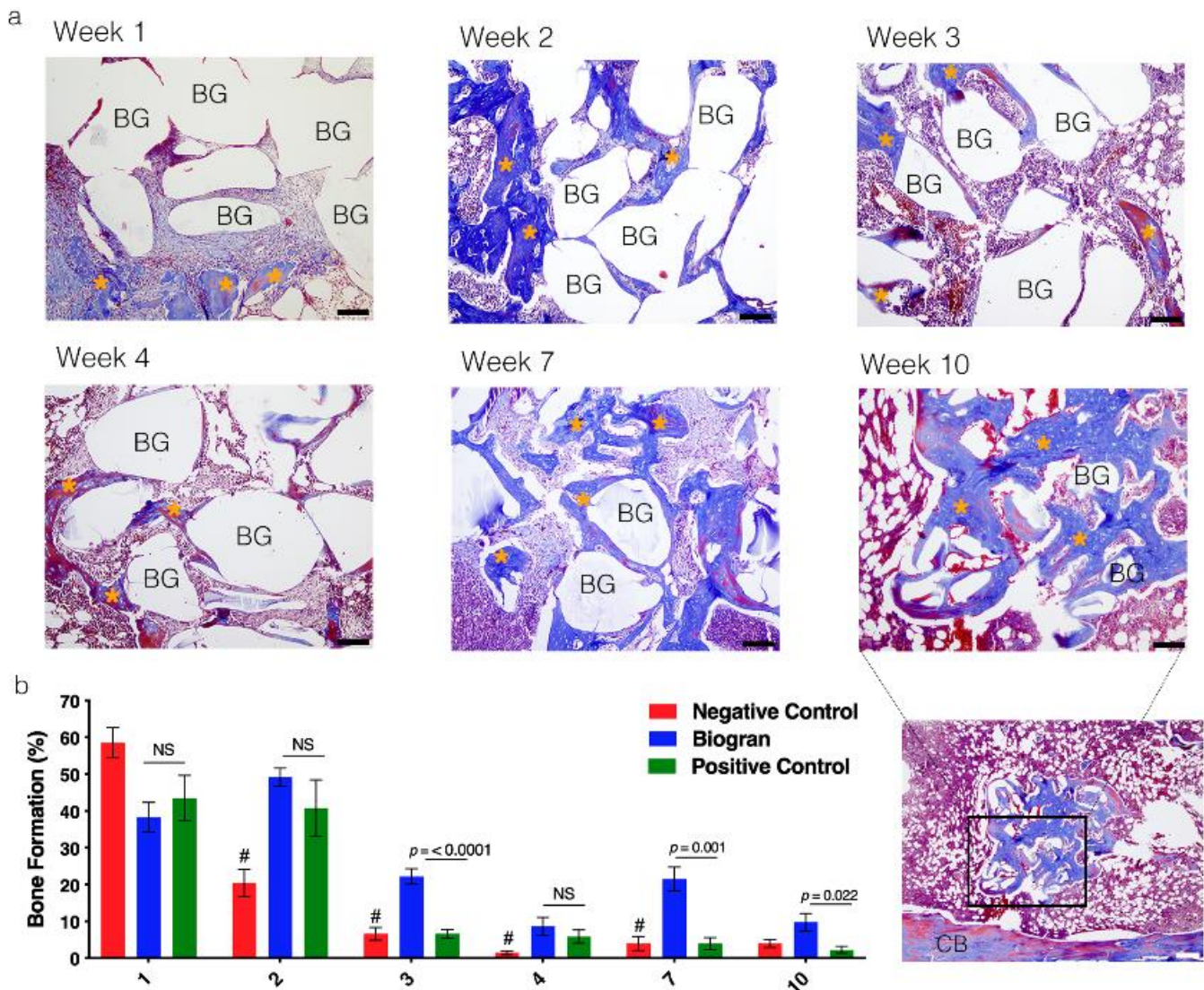


Figure 4. Representative Masson's Trichrome staining showing the bone formation and Biogran resorption cycle along the six weeks. Color bright-field photomicrographs of Biogran from the first to the 10th week (a). Note that negative images within the surgical site are corresponding to the filled biomaterial (BG). Asterisks (*) mark bone trabeculae. Bar graphs show bone neoformation quantification (1, 2, 3, 4, 7, and 10 weeks) in all groups (b). Statistically significant p values are numerically represented between Biogran and the positive control group. NS = not significant. # Shows the statistical difference between Biogran and the negative control group. Black magnification scale bars = 100 μm ; white bar = 200 μm . BG = Biogran; CB = Cortical Bone.

Biogran stimulates sustained expression of BMP-2 and presents a gradual resorption rate

The quantification of BMP-2 oscillated similarly for the control groups up to week 4 (Figure 5a). From the 4th week on, these groups presented a progressive reduction in the BMP2 concentrations. At the last experimental time, neither the negative nor the positive controls showed detectable levels of BMP-2 (Figure 5a). Overall, Biogran has stimulated sustained levels (~130 – 200 pg/100mg) of BMP-2 from the 2nd to the last experimental time, in which statistical difference was found regarding the other groups ($p < 0.0001$). The sample has presented a continuous reduction of the BMP-2 levels up to week 4, which was inversely proportional to its resorption rate (Figure 5a and b). Of note, the biomaterial's most significant resorption rate occurred within the first four weeks, when more than 80% of the Biogran was degraded (Figure 5b).

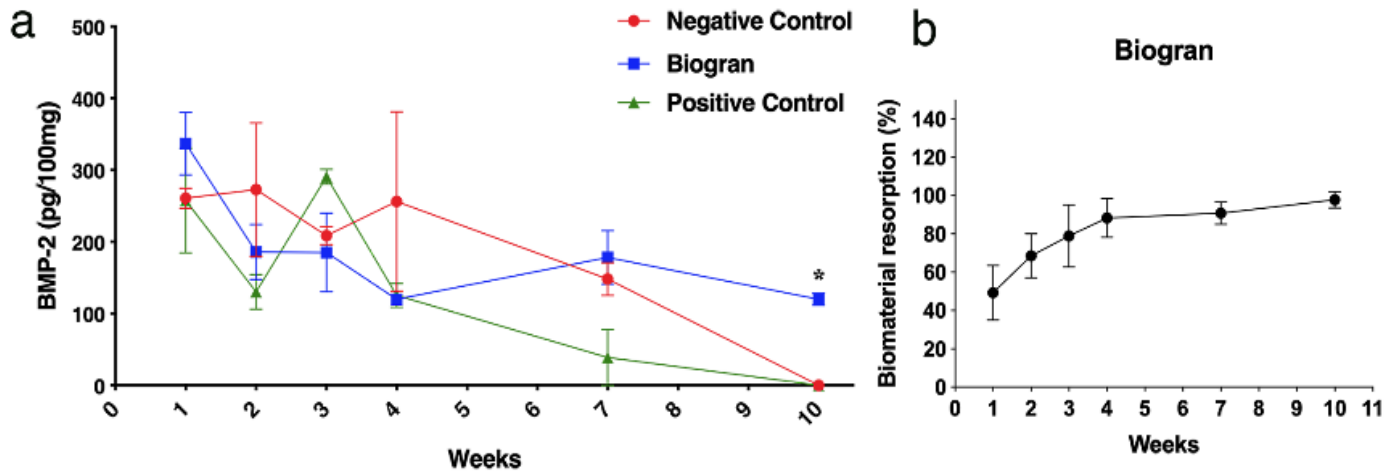


Figure 5. BMP2 expression pattern and Biogran resorption rate along the experimental times. BMP-2 expression curves along the six different experimental times (1, 2, 3, 4, 7, and 10 weeks) are shown for Biogran, positive and negative control groups (a). Asterisks (*) show greater BMP-2 expression in the Biogran concerning the controls at the last experimental time. Biogran presented around 80% of mass loss within the first month of grafting and then slowly resorbed up to the last experimental time (b).

DISCUSSION

Few studies in the literature have thoroughly characterized and evaluated the performance of the Biogran with an extended follow-up as in this work, thus allowing a comprehensive observation of the cyclic phenomena that occurred in the rat tibia bone. We have assessed Biogran as a primary source of synthetic bone engraftment for treatments within active bone remodeling sites. Our results demonstrated that the Biogran promoted sustained bone neoformation *in vivo* and allowed its resorption and substitution during bone remodeling. Concomitantly, BMP-2 was regularly stimulated in the Biogran group in a trend corresponding to the bone neoformation pattern promoted by the biomaterial. Furthermore, the Biogran grafting induced a mild inflammatory process and conferred histological characteristics similar to the autogenous bone graft control group.

SEM analysis showed that the Biogran is irregular, non-porous, and non-uniform particle size and morphology, corroborating previous reported data [43]. Surface area analysis by BET confirmed the SEM data, evidencing a dense surface texture for the biomaterial. This dense surface texture lacking micropores aligned with literature [44]. EDS and XRF data revealed the presence of silicon, sodium, calcium, oxygen, and phosphorus, as expected. These elements formed silica oxide (SiO_2), sodium oxide (Na_2O), calcium oxide (CaO), and phosphorus oxide (P_2O_5) in amounts close to a previous study [45]. The presence of these components is relevant to confer bioactivity to the glasses during dissolution in physiological conditions [1, 46]. The characterization XRD studies have shown an amorphous nature (non-crystalline) for the Biogran spectra. As the conventional melting process formed the Biogran, its oxides were subjected to a high temperature, which may justify its low porosity [47]. Surface area is known to be critical for corrosion, ion exchange, and dissolution processes and the literature reports that a surface area of 20 to 30 mg^2/g is sufficient to enhance the hydroxyapatite forming ability of particulate Biogran [48]. However, Biogran showed a low surface area and the FTIR analysis showed that the Biogran samples exhibited *in vitro* bioactivity (the appearance of HA) by increasing of bands near at 600 and 560 cm^{-1} when immersed into SBF solution. Probably, during the immersion time of the sample in the SBF solution, the dissolution was sufficient to produce pores for the growth of hydroxyapatite, thus aligning with previous works [48].

FTIR spectra of Biogran shows bands characteristic corroborating with literature [49-54]. In one day of immersion of SBF solution the band at 604 cm^{-1} was observed and could represent the presence of precursors to hydroxyapatite, either octacalcium phosphate or amorphous calcium phosphate [55]. After 3 days, the appearance of the band at 460 cm^{-1} can be explained by the loss of sodium and calcium and the formation of a silica surface layer: the band at 460 cm^{-1} is observed for pure silica [50]. The disappearance of the NBO vibrational mode near 900 cm^{-1} within the first 24 h of immersion also indicates the exchange of network modifiers (mainly sodium and calcium) with hydrogen ions from the solution and condensation of the initially formed silicon-rich surface layer [7-9]. The observed shift of transmittance from 1050 cm^{-1} to higher wavenumbers, and the broadening is suggested by an overlap of absorption due to Si–O–Si, P–O and the remaining NBO. The formation of two clearly separated bands at 600 and 570 cm^{-1} (P–O–P) confirms the existence of phosphate groups of hydroxyapatite in the sample.

The formation observed in the SEM image (Figure 2f) is attributed the presence of HA corroborating with the FTIR spectra. Many variables are known to influence the dissolution and subsequent mechanisms that lead to hydroxyapatite layer formation and bioactivity of glasses. The dissolved silicon concentration as a function of time is usually characterized by a biphasic profile, that is, the rate of dissolution is rapid at short times and slow after a time [56]. This initial loss of mass is probably due to silicon and network modifiers released into solution during the first hours. This initial fast release of ions indicates the first stage of dissolution by breaking up of the outer silica layers of the network. The solid silica dissolves in the form of monosilicic acid $\text{Si}(\text{OH})_4$ until the solution is saturated. Some authors found that silica release occurs until 1.5 h [56]. Again, in our study, the delay in forming the hydroxyapatite layer can be due to the low initial porosity of the sample. Herein, the mass loss and the rate of formation of the hydroxyapatite layer revealed a clear competition between the material dissolution and the precipitation of a CaP phase. This has also been shown by other authors [57, 58]. It appeared that, initially, there was significant dissolution of the material and, as CaP precipitates were formed, dissolution of the material, together with the dissolution of some possible amorphous precipitates, continued to occur.

Frankel and coauthors [59] reviewed the glass corrosion mechanisms and came to some conclusions: when bare glass is exposed to dilute solution, occurs rapid initial corrosion of the glass surface (Stage I) and layers on the surface begin to form (Stage II), which may protect from degradation. Stage I is controlled by hydrolysis of network forming species. In Stage II, some elements, as calcium supplied by the solution, form an amorphous, porous, and hydrated interfacial surface layer, and it appears that dissolution/precipitation dominates under conditions far from saturation (dilute condition) [60]. Similar to what was discussed by Frankel [59], the dissolution of Biogran was very fast until 3 days. Then, it decreased up to 7 days and decreased further until the end of the experiment. Regarding the formation of the HA layer, it was also very fast in up to 3 days, decreasing after that period. Confirmation of calcium phosphate layer formation was obtained by FTIR analysis.

Previous studies have shown that Biogran was intimately associated with new bone tissue formation [23, 29, 47]. Herein, the biomaterial remained in close contact with the newly formed bone for extended periods, while the autogenous bone was already reabsorbed. Interestingly, at week 7, around 90% of the biomaterial had been resorbed, where a coincident peak of bone neoformation was observed. Our *in vitro* bioactivity data resembled the *in vivo* osteoinductivity ability of the Biogran. Otherwise, these results contrast with previous reports that showed a resorption rate for the Biogran group superior concerning the autogenous bone and Biogran mixed with the autogenous bone graft (1:1) after six months of grafting in the maxillary sinus [27]. In the present study, the Biogran has shown more bone stability regarding the autogenous bone, particularly at the third week and last experimental times (7th and 10th weeks). Of note, considering the non-critical defect model used in the current study, a study limitation is that one may not confer bone neoformation ability exclusively to the biomaterial grafted.

The BMP-2 curves have fluctuated in all experimental groups. A drop in the BMP-2 expression in the Biogran group was observed at week 4. The 4th-week drop is coincident with reduced bone neoformation for the Biogran at this same experimental time. Particularly in the last two experimental times (7 and 10th weeks), BMP-2 was regularly present in the Biogran samples corroborating the sustained bone neoformation for this group. Although several other molecules may orchestrate bone remodeling, it is suggestive that the biomaterial gradually stimulates the expression of BMP-2 while being resorbed. Finally, it is worth noting that only Biogran has shown significant expression of BMP-2 at the last experimental time, which could be due to the residual ionic products released from sample remaining particles in the grafted area. In the past three years, the Biogran has been tested in different mammal models [23-26, 28, 29]. Even though several studies have investigated the Biogran behavior aiming at a craniofacial application, data about the sample engraftment into tibia defects are still scarce.

The tibia defect model has some limitations once the surgical site cannot be considered a critical size defect. However, the tibia bone presents a site-specific difference in regulating the response to mechanical loading to maintain its mass [23-26, 28, 29]. Accordingly, the tibia defect is challenging for biomaterials grafting once it may interfere in establishing an osteointegrated implant-bone interface, for example [61]. In these conditions, the biomaterial needs to resist the fast turnover displayed in long bones. Our study is the first to analyze Biogran grafting behavior in the tibia defect model.

Herein, a particular limitation is that we have used only male rats to conduct this research, which may compromise the representation of female characteristics that could interfere with the outcomes. Furthermore, bone density and volume were not evaluated through imaging assays. Altogether, our *in vivo* histological and histomorphometric analyses showed that the Biogran was well-tolerated and induced a sustained bone formation in tibia defects. Furthermore, Biogran could be a promising candidate for synthetic bone grafting in long bones or could be tested for patients affected by an adverse osteoporotic scenario [57].

CONCLUSION

Altogether, our results showed that the Biogran favored bone neoformation along with a sustained BMP-2 level within the defects, then gradually reabsorbed. The Biogran may be considered a clinically viable alternative to the autogenous grafts, even for treatments in highly active bone remodeling sites.

Funding: This work was supported in part by the Conselho Nacional de Desenvolvimento Científico e Tecnológico (CNPq #305493/2018-3, #455644/2018-1) and Coordenação de Aperfeiçoamento de Pessoal de Nível Superior (CAPES; Finance Code 001), Brazil.

Acknowledgements: L.A.Q.F. and M.S.N. are the recipients of fellowships from Fundação do Amparo à Pesquisa no Estado de Minas Gerais (FAPEMIG) and CAPES, respectively. We are thankful to the Centro de Microscopia of UFMG for SEM analysis. The Graphical Abstract was designed by modifying Smart Servier Medical Art Illustrations (<https://smart.servier.com/>).

Conflicts of Interest: The authors declare no conflict of interest.

REFERENCES

1. Lehman LFC, Noronha MS de, Diniz IMA, Costa e Silva RMF, Andrade ÂL, Lima LF de S, et al. Bioactive glass containing 90% SiO₂ in hard tissue engineering: An *in vitro* and *in vivo* characterization study. *J Tissue Eng Regen Med*. 2019;13(9):1651–63. <https://doi.org/10.1002/term.2919>
2. Nommeots-Nomm A, Labbaf S, Devlin A, Todd N, Geng H, Solanki AK, et al. Highly degradable porous melt-derived bioactive glass foam scaffolds for bone regeneration. *Acta Biomater*. 2017;57:449–61. <https://doi.org/10.1016/j.actbio.2017.04.030>
3. Baino F, Novajra G, Vitale-Brovarone C. Bioceramics and scaffolds: a winning combination for tissue engineering. *Front Bioeng Biotechnol*. 2015;3:202. <https://doi.org/10.3389/fbioe.2015.00202>
4. Hench LL, Splinter RJ, Allen WC, Greenlee TK. Bonding mechanisms at the interface of ceramic prosthetic materials. *J Biomed Mater Res*. 1971;5(6):117–41. <https://doi.org/10.1002/jbm.820050611>
5. Lopez TCC, Diniz IMA, Ferreira LS, Marchi J, Borges R, Cara SPHM de, et al. Bioactive glass plus laser phototherapy as promise candidates for dentine hypersensitivity treatment. *J Biomed Mater Res Part B Appl Biomater*. 2017;105(1):107–16. <https://doi.org/10.1002/jbm.b.33532>
6. Jones JR. Review of bioactive glass: From Hench to hybrids. *Acta Biomater*. 2013;9(1):4457–86. <https://doi.org/10.1016/j.actbio.2012.08.023>
7. Hench LL. Bioceramics. *J Am Ceram Soc*. 1998;81(7):1705–28. <https://doi.org/10.1111/j.1151-2916.1998.tb02540.x>
8. Hench LL. Biomaterials: a forecast for the future. *Biomater*. 1998;19:1419-23.
9. Hench LL. The Story of Bioglass. *J Mater Sci - Mater Med*. 2006;17(11):967–78. <https://doi.org/10.1007/s10856-006-0432-z>
10. Kokubo T, Takadama H. How useful is SBF in predicting *in vivo* bone bioactivity. *Biomater*. 2006;27(15):2907–15. <https://doi.org/10.1016/j.biomaterials.2006.01.017>
11. Kokubo T, Kushitani H, Sakka S, Kitsugi T, Yamamuro T. Solutions able to reproduce *in vivo* surface-structure changes in bioactive glass-ceramic A-W. *J Biomed Mater Res*. 1990;24(6):721–34. <https://doi.org/10.1002/jbm.820240607>
12. Cosso F, Mandia L, Lenharo A. Elevação do assoalho sinusal associado com o biomaterial “Biogran®” e instalação de implantes osseointegrados. *Innov J*. 2000;4:18–21.
13. Fooladi AAI, Hosseini HM, Hafezi F, Hosseinejad F, Nourani MR. Sol-gel-derived bioactive glass containing SiO₂-MgO-CaO-P₂O₅ as an antibacterial scaffold. *J Biomed Mater Res Part A*. 2013 Jun;101A(6):1582–7. <https://doi.org/10.1002/jbm.a.34464>

14. Johari B, Kadivar M, Lak S, Gholipourmalekabadi M, Urbanska AM, Mozafari M, et al. Osteoblast-seeded bioglass/gelatin nanocomposite: a promising bone substitute in critical-size calvarial defect repair in rat. *Int J Artif Organs*. 2016;39(10):524–33. <https://doi.org/10.5301/ijao.5000533>
15. Xynos ID, Hukkanen MV, Batten JJ, Buttery LD, Hench LL, Polak JM. Bioglass 45S5 stimulates osteoblast turnover and enhances bone formation *in vitro*: implications and applications for bone tissue engineering. *Calcif Tissue Int*. 2000;67(4):321–9. <https://doi.org/10.1007/s002230001134>
16. Gorustovich AA, Roether JA, Boccaccini AR. Effect of bioactive glasses on angiogenesis: a review of *in vitro* and *in vivo* evidences. *Tissue Eng Part B Rev*. 2010;16(2):199–207. <https://doi.org/10.1089/ten.TEB.2009.0416>
17. Nkenke E, Weisbach V, Winckler E, Kessler P, Schultze-Mosgau S, Wiltfang J, et al. Morbidity of harvesting of bone grafts from the iliac crest for preprosthetic augmentation procedures: a prospective study. *Int J Oral Maxillofac Surg*. 2004;33(2):157–63. <https://doi.org/10.1054/ijom.2003.0465>
18. Roberts TT, Rosenbaum AJ. Bone grafts, bone substitutes and orthobiologics: the bridge between basic science and clinical advancements in fracture healing. *Organogenesis*. 2012 Oct;8(4):114–24. <https://doi.org/10.4161/org.23306>
19. Schwartz CE, Martha JF, Kowalski P, Wang DA, Bode R, Li L, et al. Prospective evaluation of chronic pain associated with posterior autologous iliac crest bone graft harvest and its effect on postoperative outcome. *Health Qual Life Outcomes*. 2009 Dec;7(1):49. <https://doi.org/10.1186/1477-7525-7-49>
20. Draenert FG, Huetzen D, Neff A, Mueller WEG. Vertical bone augmentation procedures: basics and techniques in dental implantology. *J Biomed Mater Res Part A*. 2014;102(5):1605–13. <https://doi.org/10.1002/jbm.a.34812>
21. Baino F, Novajra G, Miguez-Pacheco V, Boccaccini AR, Vitale-Brovarone C. Bioactive glasses: special applications outside the skeletal system. *J Non Cryst Solids*. 2016;432:15–30. <https://doi.org/10.1016/j.jnoncrysol.2015.02.015>
22. Xu Y, Peng J, Dong X, Xu Y, Li H, Chang J. Combined chemical and structural signals of biomaterials synergistically activate cell-cell communications for improving tissue regeneration. *Acta Biomater*. 2017 Jun;55:249–61. <https://doi.org/10.1016/j.actbio.2017.03.056>
23. Gomes-Ferreira PHS, Lisboa-Filho PN, da Silva AC, Bim-júnior O, de Souza Batista FR, Ervolino-Silva AC, et al. Sonochemical time standardization for bioactive materials used in periimplantar defects filling. *Ultrason Sonochem*. 2019 Sep;56:437–46. <https://doi.org/10.1016/j.ultsonch.2019.04.032>
24. Lisboa-Filho PN, Gomes-Ferreira PHS, Batista FRS, Momesso GAC, Faverani LP, Okamoto R. Bone repair with raloxifene and bioglass nanoceramic composite in animal experiment. *Connect Tissue Res*. 2018 Nov;59(sup1):97–101. <https://doi.org/10.1080/03008207.2018.1430143>
25. Menezes JD, Pereira RS, Bonardi JP, Griza GL, Okamoto R, Hochuli-Vieira E. Bioactive glass added to autogenous bone graft in maxillary sinus augmentation: a prospective histomorphometric, immunohistochemical, and bone graft resorption assessment. *J Appl Oral Sci*. 2018 Jun;26. <https://doi.org/10.1590/1678-7757-2017-0296>
26. Pereira RS, Menezes JD, Bonardi JP, Griza GL, Okamoto R, Hochuli-Vieira E. Histomorphometric and immunohistochemical assessment of RUNX2 and VEGF of Biogran™ and autogenous bone graft in human maxillary sinus bone augmentation: A prospective and randomized study. *Clin Implant Dent Relat Res*. 2017 Oct;19(5):867–75. <https://doi.org/10.1111/cid.12507>
27. Pereira RS, Menezes JD, Bonardi JP, Griza GL, Okamoto R, Hochuli-Vieira E. Comparative study of volumetric changes and trabecular microarchitecture in human maxillary sinus bone augmentation with bioactive glass and autogenous bone graft: a prospective and randomized assessment. *Int J Oral Maxillofac Surg*. 2018;47(5):665–71. <https://doi.org/10.1016/j.ijom.2017.11.016>
28. Ruhaimi A, Khalid A. No Bone graft substitutes: a comparative qualitative histologic review of current osteoconductive grafting materials. *Int J Oral Maxillofac Implants*. 2001;16(1).
29. Zendron M, Cardoso M, Veronesi G, de Resende D, Damante C, Sant'ana A, et al. Bone Graft and Substitutes Associated with Titanium Dome for Vertical Bone Formation in Osseointegrated Implants: Histomorphometric Analysis in Dogs. *Int J Oral Maxillofac Implants*. 2018 Mar;33(2):311–8. <https://doi.org/10.11607/jomi.5762>
30. Kazemi M, Dehghan MM, Azami M. Biological evaluation of porous nanocomposite scaffolds based on strontium substituted β -TCP and bioactive glass: An *in vitro* and *in vivo* study. *Mater Sci Eng C*. 2019;105:110071. <https://doi.org/10.1016/j.msec.2019.110071>
31. Zhang Y, Cheng N, Miron R, Shi B, Cheng X. Delivery of PDGF-B and BMP-7 by mesoporous bioglass/silk fibrin scaffolds for the repair of osteoporotic defects. *Biomater*. 2012 Oct;33(28):6698–708. <https://doi.org/10.1016/j.biomaterials.2012.06.021>
32. Senta H, Park H, Bergeron E, Drevelle O, Fong D, Leblanc E, et al. Cell responses to bone morphogenetic proteins and peptides derived from them: biomedical applications and limitations. *Cytokine Growth Factor Rev*. 2009;20(3):213–22. <https://doi.org/10.1016/j.cytogfr.2009.05.00633>
33. De Caluwé T, Vercruyse CWJ, Ladik I, Convents R, Declercq H, Martens LC, et al. Addition of bioactive glass to glass ionomer cements: Effect on the physico-chemical properties and biocompatibility. *Dental Mat*. 2017;33:e186-e203.
34. Bozzola JJ, Russell LD. *Electron microscopy: principles and techniques for biologists*: Jones & Bartlett Learning; 1999.

35. Coleman NJ, Hench LL. A gel-derived mesoporous silica reference material for surface analysis by gas sorption 1. Textural features. *Ceramics Intern.* 2000;26:171-8.
36. Ullah I, Li W, Lei S, Zhang Y, Zhang W, Farooq U, et al. Simultaneous co-substitution of Sr²⁺/Fe³⁺ in hydroxyapatite nanoparticles for potential biomedical applications. *Ceramics Intern.* 2018;44:21338-48.
37. Borden M, Westerlund LE, Lovric V, Walsh W. Controlling the bone regeneration properties of bioactive glass: Effect of particle shape and size. *J Biomed Mater Res Part B: Applied Biomater.* 2022;110:910-22.
38. Domingues RZ, Clark AE, Brennan AB. A sol-gel derived bioactive fibrous mesh. *J Biomed Mater Res.* 2001 Jun;55(4):468-74. [https://doi.org/10.1002/1097-4636\(20010615\)55:4<468::AID-JBM1038>3.0.CO;2-T](https://doi.org/10.1002/1097-4636(20010615)55:4<468::AID-JBM1038>3.0.CO;2-T)
39. Serra J, González P, Liste S, Serra C, Chiussi S, León B, et al. FTIR and XPS studies of bioactive silica based glasses. *J Non Cryst Solids.* 2003;332(1-3):20-7. <https://doi.org/10.1016/j.jnoncrysol.2003.09.013>
40. Andrade VB, Sá MA, Mendes RM, Martins-Júnior PA, Silva GAB, Sousa BR, et al. Enhancement of Bone Healing by Local Administration of Carbon Nanotubes Functionalized with Sodium Hyaluronate in Rat Tibiae. *Cells Tissues Organs.* 2017;204:137-49.
41. Schallenberger MA, Rossmeier K, Lovick HM, Meyer TR, Aberman HM, Juda GA. Comparison of the Osteogenic Potential of OsteoSelect Demineralized Bone Matrix Putty to NovaBone Calcium-Phosphosilicate Synthetic Putty in a Cranial Defect Model. *J Craniofac Surg.* 2014 Mar;25(2):657-61. <https://doi.org/10.1097/SCS.0000000000000610>
42. Brovarone CV, Verné E, Appendino P. Macroporous bioactive glass-ceramic scaffolds for tissue engineering. *J Mater Sci Mater Med.* 2006;17:1069-78.
43. da Cruz ACC, Pochapski MT, Tramonti R, da Silva JCZ, Antunes AC, Pilatti GL, et al. Evaluation of physical-chemical properties and biocompatibility of a microrough and smooth bioactive glass particles. *J Mater Sci Mater Med.* 2008 Aug;19(8):2809-17. <https://doi.org/10.1007/s10856-008-3407-4>
44. Araújo MVF, Mendes VC, Chattopadhyay P, Davies JE. Low-temperature particulate calcium phosphates for bone regeneration. *Clin Oral Implants Res.* 2010 Jun;21(6):632-41. <https://doi.org/10.1111/j.1600-0501.2009.01864.x>
45. Schepers E, Clercq MD, Ducheyne P, Kempeneers R. Bioactive glass particulate material as a filler for bone lesions. *J Oral Rehabil.* 1991;18(5):439-52. <https://doi.org/10.1111/j.1365-2842.1991.tb01689.x>
46. Sharifianjazi F, Parvin N, Tahriri M. Formation of apatite nano-needles on novel gel derived SiO₂-P₂O₅-CaO-SrO-Ag₂O bioactive glasses. *Ceram Int.* 2017;43(17):15214-20. <https://doi.org/10.1016/j.ceramint.2017.08.056>
47. Rogers KD, Daniels P. An X-ray diffraction study of the effects of heat treatment on bone mineral microstructure. *Biomater.* 2002 Jun;23(12):2577-85. [https://doi.org/10.1016/S0142-9612\(01\)00395-7](https://doi.org/10.1016/S0142-9612(01)00395-7)
48. Romeis S, Hoppe A, Eisermann C, Schneider N, Boccaccini AR, Schmidt J, Peukert W. Enhancing in vitro bioactivity of melt-derived 45S5 Bioglass® by comminution in a stirred media mill. *J Am Ceram Soc.* 2014;97(1):150-6. <https://doi.org/10.1111/jace.12615>
49. Aina V, Bertinetti L, Cerrato G, Cerruti M, Lusvardi G, Malavasi G, Morterra C, Tacconi L, Menabue L. On the dissolution/reaction of small-grain Bioglass® 45S5 and F-modified bioactive glasses in artificial saliva (AS). *Appl Surf Sci.* 2011;257(9):4185-95. <https://doi.org/10.1016/j.apsusc.2010.12.019>
50. Bunker BC, Tallant DR, Headley TJ, Turner GL, Kirkpatrick RJ. The structure of leached sodium borosilicate glass. *Phys Chem Glasses.* 1988;29(3):106-20.
51. Cerruti M, Greenspan D, Powers K. Effect of pH and ionic strength on the reactivity of bioglass 45S5. *Biomater.* 2005;26(14):1665-74. <https://doi.org/10.1016/j.biomaterials.2004.07.009>
52. Onishi H, Hench LL, Wilson J, Sugihara F, Tsuji E, Matsuura M, Kin S, Yamamoto T, Mizokawa S. Quantitative comparison of bone growth behavior in granules of Bioglass®, A-W glassceramic, and hydroxyapatite *J Biomed Mater Res.* 2000;51(1):37-46. [https://doi.org/10.1002/\(sici\)1097-4636\(200007\)51:1<37::aid-jbm6>3.0.co;2-t](https://doi.org/10.1002/(sici)1097-4636(200007)51:1<37::aid-jbm6>3.0.co;2-t)
53. Pereira MM, Clark AE, Hench LL. Effect of texture on the rate of hydroxyapatite formation on gel-silica surface. *J Am Ceramics Soc.* 1995;78(9):2463-68. <https://doi.org/10.1111/j.1151-2916.1995.tb08686.x>
54. Stoch A, Jastrzebski W, Brozek A, Trybalska B, Cichocinska M, Szarawara E. FTIR monitoring of the growth of the carbonate containing apatite layers from simulated and natural body fluids. *J Mol Struct* 1999;511-512:287-94.
55. FitzGerald V, Martin RA, Jones JR, Qiu D, Wetherall KM, Moss RM, et al. Bioactive glass sol-gel foam scaffolds: evolution of nanoporosity during processing and in situ monitoring of apatite layer formation using small- and wide-angle X-ray scattering. *J Biomed Mater Res Part A* 2009;91A:76-83.
56. Sepulveda P, Jones JR, Hench LL. *In vitro* dissolution of melt-derived 45S5 and sol-gel derived 58S bioactive glasses. *J Biomed Mater Res.* 2002;Aug;61(2):301-11. <https://doi.org/10.1002/jbm.10207>
57. Wang N, Niger C, Li N, Richards GO, Skerry TM. Cross-Species RNA-Seq Study Comparing Transcriptomes of Enriched Osteocyte Populations in the Tibia and Skull. *Front Endocrinol (Lausanne).* 2020 Sep;11. <https://doi.org/10.3389/fendo.2020.581002>
58. Eliaz N, Metoki N. Calcium phosphate bioceramics: a review of their history, structure, properties, coating Technologies and Biomedical Applications. *Mater.* 2017;10:334. <https://doi.org/10.3390/ma10040334>
59. Frankel GS, Vienna JD, Lian J, Scully JR, Gin S, Ryan JV, et al. A comparative review of the aqueous corrosion of glasses, crystalline ceramics, and metals. *NPJ Mater Degrad.* 2018 Dec;2(1):15. <https://doi.org/10.1038/s41529-018-0037-2>

60. Geisler T, Janssen A, Scheiter D, Stephan T, Berndt J, Putnis A. Aqueous corrosion of borosilicate glass under acidic conditions: A new corrosion mechanism. *J Non Cryst Solids*. 2010 Jun;356(28–30):1458–65. <https://doi.org/10.1016/j.jnoncrysol.2010.04.033>
61. Mondal S, Ghosh R. The effects of implant orientations and implant–bone interfacial conditions on potential causes of failure of tibial component due to total ankle replacement. *J Med Biol Eng*. 2019;39(4):541–51. <https://doi.org/10.1007/s40846-018-0435-5>



© 2024 by the authors. Submitted for possible open access publication under the terms and conditions of the Creative Commons Attribution (CC BY NC) license (<https://creativecommons.org/licenses/by-nc/4.0/>).